Analytical and Bioanalytical Chemistry (2019) 411:5393–5403
https://doi.org/10.1007/s00216-018-1378-y

RESEARCH PAPER

An investigation into the kinematics of magnetically driven droplets on various (super)hydrophobic surfaces and their application to an automated multi-droplet platform

Prashant Agrawal[1] · **Kyle J. Bachus**[1] · **Gabrielle Carriere**[1] · **Phoenix Grouse**[1] · **Richard D. Oleschuk**[1]

Received: 19 July 2018 / Revised: 6 September 2018 / Accepted: 13 September 2018 / Published online: 5 October 2018

Abstract

Magnetic actuation on digital microfluidic (DMF) platforms may provide a low-cost, less cumbersome alternative for droplet manipulation in comparison to other techniques such as electrowetting-on-dielectric. Precise control of droplets in magnetically driven DMF platforms is achieved using a low-friction surface, magnetically susceptible material/droplet(s), and an applied magnetic field. Superhydrophobic (SH) surfaces offer limited friction for aqueous media as defined by their high water contact angles (WCA) (>150°) and low sliding angles (<10°). The low surface friction of such coatings and materials significantly reduces the force required for droplet transport. Here, we present a study that examines several actuation parameters including the effects of particle and particle-free actuation mechanisms, porous and non-porous SH materials, surface chemistry, droplet speed/acceleration, and the presence of surface energy traps (SETs) on droplet kinematics. Automated actuation was performed using an XY linear stepper gantry, which enabled sequential droplet actuation, mixing, and undocking operations to be performed in series. The results of this study are applied to a quantitative fluorescence-based DNA assay in under 2 min.

Keywords Magnetic actuation · Superhydrophobic · Droplet · DNA quantitation

Introduction

A superhydrophobic (SH) surface, defined by a water contact angle (WCA) >150° and a sliding angle <10°, is a result of stronger cohesive forces within the molecules of the droplet resting on the surface compared to weak adhesive forces acting between the droplet and the surface material [1]. In 1997, Barthlott and Neinhuis performed a systematic study highlighting the super water-repellent and self-cleaning ability of the lotus leaf (*Nelumbo nucifera*) and attributed the observed superhydrophobicity to nano- and microscale waxy surface texture [2]. Since that study, there have been many techniques applied to the fabrication of SH surfaces [3–7]. Sun et al. [8] created a replica of the lotus leaf via a casting approach using PDMS to produce a substrate with the same surface morphology as the lotus leaf and a WCA of 160°. Alternatively, Lee et al. [9] utilized nanoimprint lithography to pattern polystyrene substrates with different nanostructures resulting in an SH surface. More recently, porous polymer monolithic (PPM) coatings have emerged as a pathway towards superhydrophobic-superhydrophilic micropatterns [10–12]. Levkin et al. [13] reported the fabrication of SH PPM coatings on flat substrates with WCAs as high as 172°. Material synthesis involved injecting a polymerization solution into the void generated by a thin spacer between two vinyl-functionalized glass plates and polymerizing under ultraviolet radiation. In this case, the material (coating) thickness is controlled using a spacer separating the two plates and WCA can be controlled by monomer selection and porosity tuning [14].

Interest in SH materials has led to the development of surfaces with spatial control over relative surface energy. Surfaces with patterned wettability have been utilized for applications including water harvesting, anti-icing, anti-fogging, and drug release [15–17]. The wetting of droplets on hydrophilic regions of a surface significantly increases droplet–

Published in the topical collection *Ultrasmall Sample Biochemical Analysis* with guest editors Ryan Kelly and Ying Zhu.

Electronic supplementary material The online version of this article (https://doi.org/10.1007/s00216-018-1378-y) contains supplementary material, which is available to authorized users.

✉ Richard D. Oleschuk
richard.oleschuk@chem.queensu.ca

[1] Department of Chemistry, Queen's University, 90 Bader Lane, Kingston, ON K7L 3N6, Canada

surface adhesion, and when a sufficiently sized surface energy trap (SET) is employed, the droplet can be pinned in place [18]. Depending on the adhesive forces, the droplet can be released from the SET using an applied force, which has been used for liquid dispensing [19]. Patterned surfaces can be prepared by methods such as laser micromachining, photopatterning, and micro-contact spotting [20, 21]. In particular, laser micromachining is an attractive approach for rapid prototyping of patterned surfaces with high fidelity [19].

In addition to self-cleaning, low adhesion and patterned surfaces have also found applications in digital microfluidic (DMF) devices [11, 22–24] where small volume liquid droplets (on the order of microliters (μL) to picoliters (pL)) are actuated, mixed, merged, split, and analyzed on micro-patterned substrates [14]. In many cases, facilitating the fundamental operations requires a surface with low friction (adhesion). Magnetic actuation is an emerging DMF method that uses droplets containing a magnetically susceptible material (on a low friction SH surface) in combination with an applied external magnetic field [25]. In many cases, the magnetically susceptible material is in the form of superparamagnetic particles [26, 27], and more recently, paramagnetic salts have been employed and manipulated with either permanent [28] or electromagnets [29].

A detailed study has been done by Long et al. to characterize droplet movement, coalescence, and splitting on a hydrophobic surface [30]. Droplets on SH surfaces in a Cassie–Baxter state exhibit significantly lower sliding angles compared to hydrophobic surfaces. The decreased friction between the droplet and surface reduces the magnetic force required for droplet movement. As a result, lower amounts of particles are required and even materials with relatively low magnetic susceptibility (i.e., paramagnetic salts) can be employed for magnetic actuation. Furthermore we utilize laser micromachining to produce SETs to position and park droplets which can later be picked up via a magnetically actuated droplet. This report is the first to focus upon the combination of magnetic actuation and SETs to carry out droplet merging, mixing, and detection for a DNA-based assay. DNA quantitation using the fluorochrome Hoechst 33258 (bisbenzimide) is a simple and sensitive method [31, 32]. The Hoechst 33258 dye has a preference for A–T base pairs in DNA and in particular binds to its minor groove with high selectivity [32, 33] even in the presence of RNA, proteins, nucleotides, and dilute buffer reagents [34, 35]. Alternatively, DNA detection in a droplet-based microfluidic devices has recently been published by Chen et al. which employed a continuous flow device with quantum dots [36]. Their study, however, required more complex chip fabrication and fluid control architecture.

Actuation performance is tested on Ultra-Ever Dry, a fluorinated PPM and a “fluorine-free” PPM surface [13]. Droplet kinematics and the disengagement forces for droplets resting on laser-ablated SETs are assessed using a programmable XY stage. The effect of droplet size and concentration of salt/particles on droplet disengagement acceleration was systematically examined on all surfaces. Using the optimized particle concentration, SET diameter, and the appropriate SH surface, a sequential quantitative droplet-based DNA assay is performed. The conventional methods for DNA quantitation can take up to 10 μL of DNA and 2 mL of dye sample for analysis, are time consuming, and require a fluorometer and manual sample preparation. In this work, we present a method which reduces the amount of analyte consumed, reduces the time taken for analysis, takes away the need for a fluorometer, and automates sample preparation.

Materials and methods

Materials

Glass microscope slides were purchased from Fisher Scientific (Economy Plain Glass Micro Slides; 76 × 25 × 1 mm) and were used as substrates. For DNA quantitation and sequential droplet actuation studies, larger (102 × 76 × 1 mm) slides were used (Ted Pella, Inc). Ultra-Ever Dry™ was obtained from Hazmasters (Ottawa, Canada). 1H,1H-Heptafluoro butyl acrylate (FBA) was sourced from Oakwood Chemicals. 2,2-Dimethoxy-2-phenylacetophenone (DMPAP), 3-(trimethoxysilyl)propyl methacrylate (γ-MAPS), benzophenone, butyl methacrylate (BuMA), cyclohexanol, decanol, ethylene glycol dimethacrylate (EDMA), trichloro(1H,1H,2H,2H-perfluorooctyl)silane, hydroxyethyl methacrylate (HEMA), manganese(II) chloride tetrahydrate, and *tert*-butanol were all purchased from Sigma-Aldrich. All monomers were used without removal of inhibitors. Acetic acid was obtained from Fisher Scientific. Acetone and methanol were purchased from ACP Chemicals. Particles were obtained from Bioclone Inc. (San Diego, USA). The particles have a diameter of ~1.0 μm, magnetization of ~40 emu/g, and an iron oxide core, which is coated with a layer of silica. The NdFeB cylindrical magnets used for actuation were purchased from K&J Magnetics, Inc., PA. The magnetic field strength of the magnet was measured to be 5.64 kG before and 3.24 kG after placing a glass slide (1 mm thick) between the gaussmeter probe (Gaussmeter Model 410, LakeShore Cryotronics Inc., Westerville, OH) and the magnet. Fluorescence DNA quantitation kit including calf thymus DNA and Hoechst 33258 dye was purchased from BIO-RAD. This article does not contain any studies with human participants or animals performed by any of the authors.

Ultra-Ever Dry™ preparation and application

Ultra-Ever Dry (UED) is a two-layer superhydrophobic coating, and each layer was applied separately as an aerosol as per the manufacturer’s instructions. The first layer is an adhesive polymer layer while the second layer is comprised of fluorinated silica nanoparticles. The UED coating exhibits water contact angles >160° and sliding angles <1°. Typically, the slides were left under ambient conditions to dry for a minimum of 20 min before the application of the second layer and further dried overnight before use.

Porous polymer monolith synthesis on a planar substrate

A procedure described by Levkin et al. [13] was followed to prepare PPMs on glass substrates. First, clean glass slides were activated by exposure to 1 M NaOH for 30 min followed by exposure to 1 M HCl for 30 min. After activation, the slides are functionalized following a previously developed protocol [13]. The functionalization mixture comprises 20% v/v solution of γ-MAPS in ethanol and adjusted to pH 5 by the dropwise addition of acetic acid. This mixture is applied to the top of a glass slide, and another glass slide is placed on top. The slides are functionalized for 60 min with re-application of functionalization solution after 30 min. After functionalization, the slides are thoroughly rinsed with both methanol and acetone and dried under nitrogen. All glass slides were kept in a desiccator and used within a 4-day period.

Thin strips of Teflon® (50 μm; McMaster-Carr) were cut and placed along the long edges of a functionalized glass slide. The pre-polymer mixture was applied to the slide with a disposable pipette, followed by placing another slide on top of the bottom slide and purged of air bubbles. The assembly forms the template while the thin strips define the thickness of the final material. The slides are fastened together with four pressure clips to maintain slide position during polymerization.

Following template assembly (filled with pre-polymer mixture) (Table 1), the template is placed under an ultraviolet lamp (254 nm) for 30 min. After polymerization, the clips and Teflon® strips are removed, and the glass slides are carefully disassembled using a sharp blade. Lastly, the material is thoroughly washed with methanol and acetone, and dried under nitrogen flow.

For photografting, HEMA-PPM is left to soak in methanol for 1 h to remove unreacted monomer. Effective photografting requires repeating the sandwiched template approach with a fluorinated top plate [21]. To fluorinate the top plate, an activated glass slide is placed in a desiccator with ~50 μL of trichloro(1H,1H,2H,2H-perfluorooctyl)silane for 12 h where chemical vapor deposition facilitates complete coverage of the fluorinated silane [13]. The HEMA substrate is saturated with FBA photografting solution within the fluorinated template and polymerized/rinsed as described above (Table 1).

Laser micromachining

Laser micromachining was performed using an Oxford Lasers A Series Compact Micromachining System, equipped with a 355-nm solid-state diode-pumped picosecond-pulsed laser. The laser was operated at a power of 45.7 ± 4.5 mW. The associated software uses G-code programs to manipulate an XY stage and laser optics (in Z) to perform the machining. Programs were created to mill circles in a substrate with the ability to vary the size and spacing of the array, the circle diameter. The code was written such that the laser would write concentric circles starting from the outermost circle (equal to the programmed diameter) and moving inward by the defined pitch, with a small spot to fill in the core of the circle.

The superhydrophobic-coated substrate is placed inside the enclosure of the laser micromachining system and fixed onto the XY stage using tape to prevent any movement while the stage is in motion. The substrates bearing hydrophilic SETs are washed with deionized water after removal from the laser micromachining chamber before use. SETs with diameters of 250 and 1000 μm at a milling speed of 0.5 mm/s with a 10-μm pitch were machined into the superhydrophobic surface following a method previously developed by Bachus et al. [19]. Center to center SET spacing was chosen to match the magnet pitch.

Water contact and sliding angle characterization

Rapid measurements of WCA and SA of surfaces were made using a USB microscope (Veho VMS004D) and ImageJ software. When necessary, more precise measurements were carried out using a Dataphysics OCA 15Pro optical contact angle measuring system.

Magnetic actuation

For magnetic actuation, magnetically susceptible material within a droplet creates a "responsive" material which facilitates droplet movement in the presence of a magnetic field. Paramagnetic salts (such as $MnCl_2 \cdot 4H_2O$) and particles are two types of magnetically susceptible materials that can be introduced into a droplet to generate magnetically responsive droplets. The way in which these materials interact with aqueous media presents an interesting difference in their actuation mechanisms.

Aqueous solutions of 1–4 M $MnCl_2$ and particle solutions of 1–4 mg/mL were prepared in small vials. During the preparation of the particle solutions, the particles were extensively washed with water. Magnetic actuation was carried out by programming an XY stage (H2W Technologies) equipped with a magnet array (Fig. 1). Additional information on the coding (see Electronic Supplementary Material (ESM); ESM-1 Table S1) and stage movement are presented in the electronic supplementary information (see ESM-1 Fig. S1). As can be seen in ESM-1 Fig. S1, the stage's velocity only changes while the stage is either accelerating or decelerating. Hence we chose to study droplet

Table 1 Abbreviations and solution compositions for the polymer monolith synthesis

Abbreviation	Initiator	Monomer/cross-linker composition	Solvent
Low density BuMA-*co*-EDMA	DMPAP (1 wt.%)	20 wt.% BuMA and 30 wt.% EDMA	40 wt.% decanol and 10 wt.% cyclohexanol
High density BuMA-*co*-EDMA	DMPAP (1 wt.%)	20 wt.% BuMA and 30 wt.% EDMA	25 wt.% decanol and 25 wt.% cyclohexanol
HE-*co*-EDMA	DMPAP (1 wt.%)	20 wt.% HE and 30 wt.% EDMA	25 wt.% decanol and 25 wt.% cyclohexanol
FBA photografting solution	Benzophenone (0.25 wt.%)	15 wt.% FBA and 1 wt.% EDMA	84 wt.% 3:1 *t*-BuOH/water (v/v)

disengagement acceleration as an actuation parameter. To optimize the sequential droplet actuation parameters, independent studies were performed on each of the hydrophobic and superhydrophobic coatings using droplets containing paramagnetic salts and particles separately.

DNA quantitation sample preparation

Seven standard solutions (1 μL total volume) of calf thymus DNA were prepared with concentrations between 0 and 1000 μg/mL to perform the DNA quantitation via fluorescence. Seven solutions (20 μL), each containing 10 μg/mL of the Hoechst dye and 2 mg/mL of the particles, were mixed and placed on each of the SETs. The intercalating dye enables the DNA to be detected at (375 nm excitation and 480 nm emission). This detection is further explained later.

Results and discussion

Development of porous polymer monoliths

A PPM is a material comprised of an extensive, interconnected network of polymer globules [37]. Pores in the structure are a result of solvophobic interactions between the porogenic solvents and the partitioning polymer [38]. Several groups have investigated templated, in situ photopolymerizations to synthesize PPM materials in narrow bore capillaries and optical fibers [38, 39]. Similar polymerization chemistry can be utilized to functionalize a planar surface with a PPM, where material composition and surface roughness dictate wetting and sorption properties. Levkin et al. [13] have used this technique extensively for the fabrication of superhydrophobic porous polymer coatings. Here, we also implement this approach to produce PPM coatings [13] (Sect. "Porous polymer monolith synthesis on a planar substrate") and compare the feasibility of microfluidic operations on these surfaces to commercially available UED coatings.

Glass substrates coated with PPM and UED were chosen to examine the effect of porosity on magnetic actuation of paramagnetic salt and particle-containing droplets. Scanning electron micrographs in Fig. 2e–g show that all the coatings have differing surface structure. The nano-roughness required to impart superhydrophobicity for PPMs arises from the template disassembly after the polymerization. The nano-roughness for UED coatings, however, arises from the presence of silica nanoparticles on the top layer [13]. Porosity and density of a PPM material are inversely proportional, and throughout this work, PPMs will be compared with respect to their densities (Fig. 2e and f). A low-density BuMA-*co*-EDMA PPM (Table 1) and a high-density analogue were developed (Fig. 2e and f). The low-density monolithic coating produced a material with WCA angle of 143° ± 1° compared to that of the high-density coating, which had a WCA of 145° ± 3°. While avoiding fluorinated material promotes a more cost-effective and environmentally friendly approach to material synthesis, the water contact angles did not satisfy the superhydrophobic criterion. Out of interest, the material was still considered for actuation testing. The fluorinated coating (Fig. 2g) is the only PPM-based coating that satisfied the superhydrophobic criterion owing to its WCA of 151.6° ± 0.6° and SA of 4.3 ± 1.5°. Images of 5-μL water droplets on each of the PPM and UED coatings can be found in Fig. 2a–d with associated scanning electron micrographs of the surface.

Magnetic actuation on (super)hydrophobic surfaces

When paramagnetic salts are introduced in aqueous media, the salt dissolves and results in homogeneous dispersion of magnetic material within a droplet in the presence and absence of an applied magnetic field. In this case, the entire droplet is responsive to the applied magnetic field. Conversely, the particles form a suspension and are attracted to the area of the droplet in the direction of the magnetic field; in this case, the particles agglomerate at the bottom of the droplet as the magnetic field is applied from below the substrate. As the magnet is translated under the substrate, the particles are constrained within the droplet because of surface tension and create a moveable particle "raft" for the aqueous droplet to travel along. In this case, the droplet will remain attracted to the magnetic field so long as the surface tension is not overcome by other active forces such as gravity, inertia, and momentum. The strength of the magnetic "raft" between the droplet and the magnetic field also depends on the magnetic susceptibility of the materials and these are summarized in Table 2.

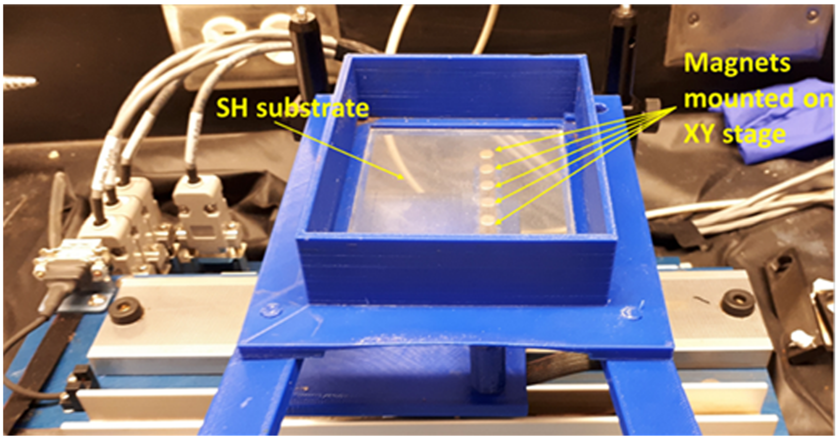

Fig. 1 Photograph of the magnetic actuation assembly. The magnets are visible under the SH surface and are mounted on the XY stage. The SH-coated glass substrate can be seen resting on a 3D-printed holder

During actuation, the droplet can disengage from the magnet if the frictional force, F_f and maximum capillary force, $F_{c,max}$ exceed the maximum magnetic force, $F_{m,max}$ [30]. The frictional force can be described as

$$\overrightarrow{F_f} \cong K_f R_b U \tag{1}$$

where K_f is a friction constant, R_b is the radius of the bottom contact area between the droplet and the surface, and U is the droplet velocity, and the maximum capillary force is given by

$$\overrightarrow{F}_{c,max} = 6^{\frac{1}{3}}\pi^{\frac{2}{3}}\Upsilon V^{\frac{1}{2}} \tag{2}$$

where V is the volume of the magnetic "responsive" material inside the droplet and γ is the interfacial tension between the bulk of droplet and the outside medium, i.e., water–air interface. Capillary force is generated by the droplet deformation caused by magnetic "responsive" material pressing against the side of the droplet in the direction of magnet travel away from the droplet. The $F_{c,max}$ term characterizes the particle extraction and is related to the volume of the particles. The capillary force generated during magnetic actuation using particles is due to the formation of an agglomerated bead-cluster which carries the droplet. If the magnetic force exceeds the maximum capillary force ($F_{c,max}$) then the agglomerated particles are extracted from the droplet. In droplets containing salt, bead-cluster formation is not possible as the salt is completely dissolved (i.e., hydrated ions) and homogeneously distributed within the droplet. Lack of a bead-cluster prevents the possibility of particle extraction. As a result, $F_{c,max}$ is not appropriate for droplets containing paramagnetic salt. The magnetic force that must overcome the frictional as well capillary force is described as $\overrightarrow{F}_m$:

$$\overrightarrow{F}_m = V\chi(Bm/\mu_o)\nabla\overrightarrow{B}_m \tag{3}$$

$$\overrightarrow{F}_{m,max} = \overrightarrow{K}_{m,max}\chi V \tag{4}$$

where χ is the magnetic susceptibility of the magnetic material, B_m is the strength of the applied external field, μ is the permittivity of free space, and $K_{m,max}$ is the maximum value of $(Bm/\mu\ )\nabla B_m$ that can be achieved for a given magnetic actuation device.

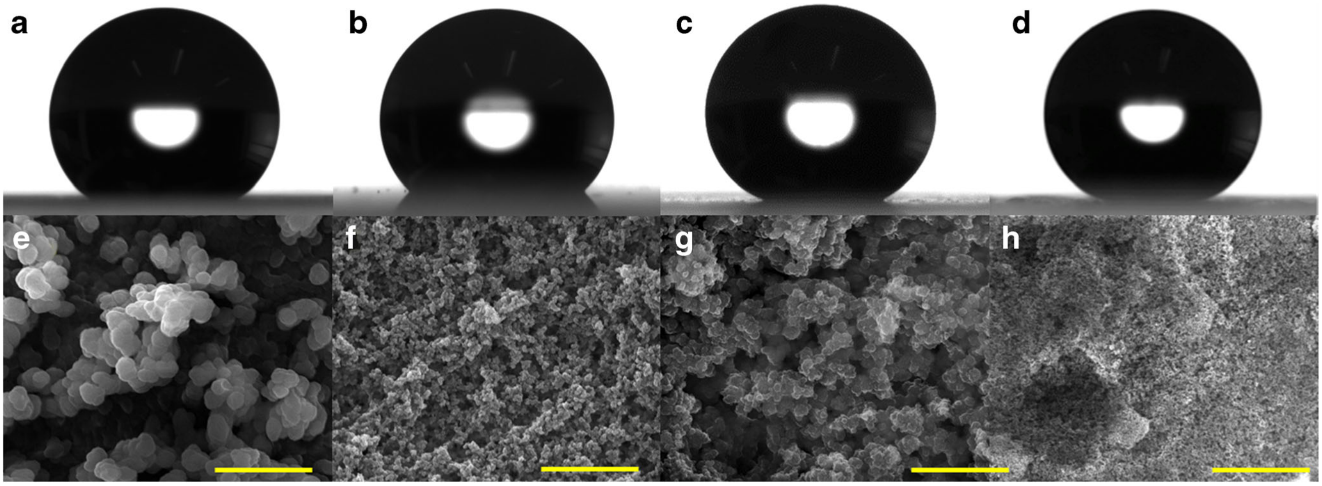

Fig. 2 Images of 5-μL water droplets on and SEMs of **a**, **e** high density BuMA-*co*-EDMA, **b**, **f** low density BuMA-*co*-EDMA, **c**, **g** FBA-*co*-EDMA, and **d**, **h** Ultra-Ever Dry. Scale bars are all 5 μm

Table 2 Magnetic susceptibility and amounts used for the materials

Magnetic material	Magnetic susceptibility (cm^3/mol) [26]	Material concentration (mg mL^{-1})
$MnCl_2 \cdot 4H_2O$	$13{,}250 \pm 280 \times 10^{-6}$	197.91 to 791.64
Particle	10^{-2} to 10^2	1 to 4

A parametric study was conducted on all (super)hydrophobic coatings to determine the acceleration at which a droplet disengages from the magnet as a function of droplet volume, paramagnetic salt concentration, mass of particles, and morphological/chemical properties of the substrate material. The acceleration data outlines boundary conditions for analytical droplet operations. In particular, the paramagnetic salt ($MnCl_2 \cdot 4H_2O$) and the particles were independently evaluated for all four surfaces at seven different concentrations and four different volumes. Figure 3 shows the droplet actuation performance for the UED-coated sample. UED exhibits the highest contact angles and lowest sliding angle of the coatings tested.

Droplet acceleration is dependent upon paramagnetic salt (solid lines, Fig. 3) concentration where droplets containing higher salt concentrations tolerate increased acceleration without disengagement (Eqs. 1, 2, and 3) (see ESM-2). Furthermore, droplets with salt concentrations 2 M and above (Fig. 3) did not disengage on the UED surface at the highest acceleration (1.2 m/s^2) tested. For particle-based actuation (dashed lines, Fig. 3), an increase in droplet disengagement acceleration was observed when particle concentration is increased from 1 to 1.5 mg/mL. However, contrary to the salt-based actuation, increasing the particle concentration beyond 1.5 mg/mL does not result in a significant increase in droplet disengagement acceleration. It follows then that droplet volumes with particle concentrations from 1.5 to 4 mg/mL have attained a critical concentration such that increasing particle concentration further will have a negligible effect on droplet disengagement acceleration within the tested regime.

The droplet mass is an essential parameter for droplet disengagement (Eq. 1). For UED, droplets with higher volumes, i.e., greater mass, disengage at lower acceleration when using both salt and particles. Droplet disengagement was observed for the 1 M and 1.5 M salt concentrations, and maximum droplet disengagement acceleration decreased with increasing droplet volume. This can be explained using Eqs. 1, 2, and 3. It is evident from Eq. 3 that F_m increases with an increase in the droplet volume. An increase in volume is also responsible for an increase in $F_{c,max}$ and F_f (increase in R_b) (Eqs. 1 and 2). Hence, it is possible that the combined effect of an increase in $F_{c,max}$ and F_f is greater than the increase in F_m which results in a decrease in droplet disengagement acceleration. We observed a similar trend for particle droplet actuation. However, the impact of droplet volume is more pronounced: 40-μL droplets could not be accelerated with particle concentrations of 2.5 mg/mL or less, which is presumably a result of the ratio between "raft" mass and droplet mass.

Although particles have been utilized for droplet manipulation on other hydrophobic and superhydrophobic surfaces, particle-based actuation was not possible on the PPM coatings studied here (see ESM-3) (Fig. 4a–c) [40–42]. The presence of a magnetic field causes any particles within a droplet to both aggregate and move toward the magnet, which in the case of the PPM coatings (low and high density) causes entrapment of the particles in the larger pores of the material and ultimately causes droplet pinning. Once the magnetic field has been applied and subsequently removed, the droplet remains pinned on the PPM substrate under complete inversion of the platform (see ESM-1 Fig. S2).

Figures 4a–c show that in most salt-based actuation cases, droplet disengagement acceleration increases with an increase in droplet volume until 30 μL. The increase is attributed to the more magnetically responsive material being available, i.e., larger handle (Eqs. 2 and 3). An increase in volume causes increases in F_m and F_f. In this case, it is possible that the effect of an increase in F_f is less than the increase in F_m which increases droplet disengagement acceleration. At volumes beyond 30 μL the droplet disengagement acceleration remains constant or decreases. A possible explanation for this behavior is that at larger volumes F_f is greater than F_m because of a more substantial increase in R_b compared to increase in the volume of the droplet. The more substantial increase in R_b is due to the gravitational pull on the droplet.

Although low density BuMA-*co*-EDMA and high density BuMA-*co*-EDMA had statistically the same WCA, low density

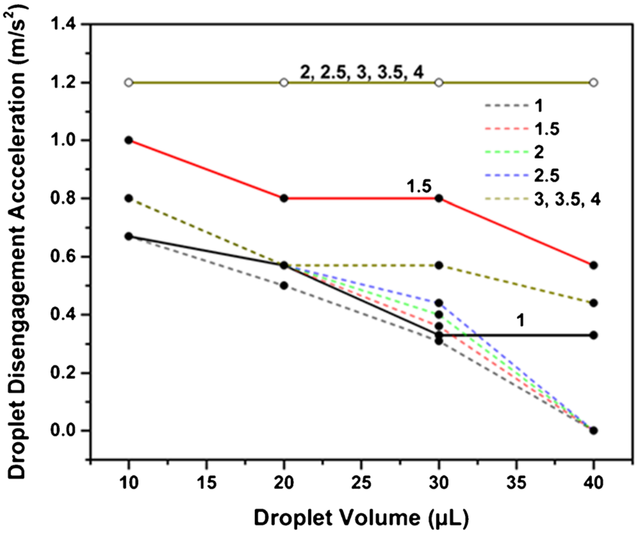

Fig. 3 Particle and $MnCl_2 \cdot 4H_2O$ droplet disengagement at different accelerations and volumes on UED. The dashed lines represent particle-based actuation while the solid lines represent salt-based actuation. The labels on the curves represent concentrations of particles (in mg/mL) and salts (in M). Open circles represent droplets which do not disengage at the highest tested acceleration (1.2 m/s^2) while solid circles represent droplets which disengage at the respective acceleration

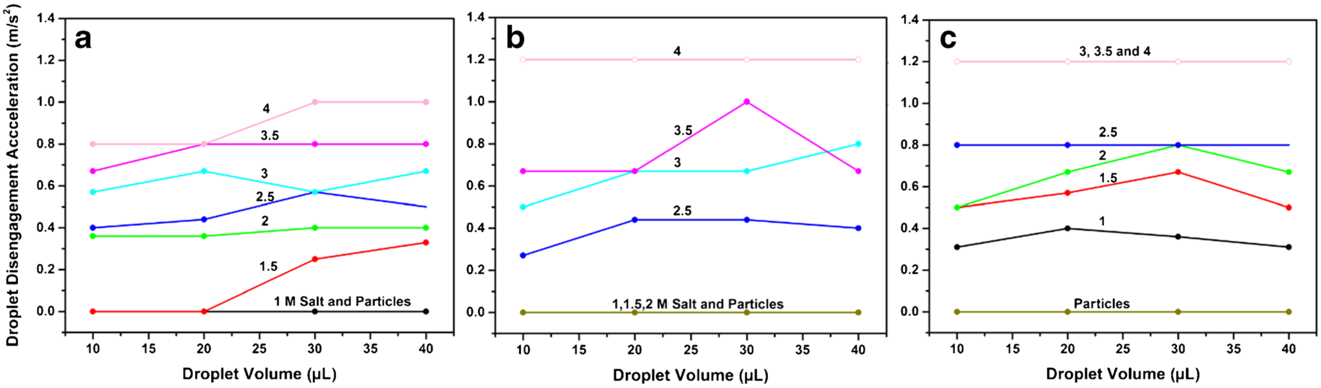

Fig. 4 Particle and $MnCl_2{\cdot}4H_2O$ droplet disengagement at different accelerations and volumes on **a** FBA-*co*-EDMA, **b** low density BuMA-*co*-EDMA, and **c** high density BuMA-*co*-EDMA. For all conditions tested, particle containing droplets on PPM surfaces were not actuated, shown as a flat line at 0.0 m/s^2. The numerical labels on the curves represent concentrations of salt (in M). Open circles represent droplets that do not disengage at the highest tested acceleration (1.2 m/s^2) while solid circles represent droplets that disengage at the acceleration indicated

BuMA-*co*-EDMA coating showed the lower droplet disengagement acceleration of the two PPMs. This result is likely due to the difference in their sliding angles. The siding angle for low density BuMA-*co*-EDMA is >40°, but for high density BuMA-*co*-EDMA it is 8 ± 3°. Sliding angle is directly proportional to F_f; a higher SA for low density BuMA-*co*-EDMA translates into higher F_f which results in lower droplet disengagement accelerations (i.e., the less slippery surface results in the earlier disengagement of the droplet from the magnet). Similarly, the FBA-*co*-EDMA coating having higher WCA (151.6° ± 0.6°) and lower sliding angle (4.3° ± 1.5°) than high density BuMA-*co*-EDMA (145.0° ± 3.0°/8.0° ± 3.0°) shows higher droplet disengagement accelerations. On the basis of the discussion above, UED shows superior performance for salt and particle-mediated magnetic actuation. Droplets could be accelerated and decelerated as quickly as 1.4 m/s^2 with particle and salt concentrations as low as 1 mg/mL and 1 M, respectively. Force analysis diagrams for droplet actuation on SH surfaces are provided in the electronic supplementary information (ESM-1 Figs. S4 and S5). UED was consequently chosen to conduct experiments that enabled a droplet to be docked and undocked on SETs patterned on the surface.

Docking and undocking droplets from SETs

Generating hydrophilic regions (i.e., SETs) on an otherwise superhydrophobic surface is essential for many applications including water harvesting, small-volume deposition, and droplet pinning [14]. In our application, we utilize SETs to temporarily anchor or "dock" droplets, ease droplet placement on the SH surface, and position the droplets at regular intervals that correspond with permanent magnet spacing on the XY stage (see ESM-3). UED-coated slides were laser micromachined with 250- and 1000-μm diameter SETs following a previously reported method [19]. Figure 6 shows a scanning electron micrograph of a typical 250-μm SET. A systematic study was performed to understand the effects of salt/particle concentration, droplet volumes, SET size, and acceleration on the magnetically induced undocking of droplets from the SETs using the XY stage.

To undock a droplet from a SET, the adhesive force, F_{adh}, must be overcome. The adhesion force of a droplet placed on the SET can be estimated with a sliding angle experiment by $F_{adh} = mg \sin\theta$, where θ is the sliding angle, m is mass of the droplet, and g is acceleration due to gravity. The adhesion force for 20-μL droplets placed on 250- and 1000-μm SETs was found to be 57 ± 2 and 166 ± 8 μN respectively, not surprisingly indicating that the adhesion force increases with an increase in SET diameter. Under these magnetic actuation conditions, the adhesive force of the 1000-μm patch (166 μN) was too large to overcome and thus prevented any undocking of droplets. It was possible to undock droplet volumes 20–40 μL with particle concentrations ≥2 mg/mL, using accelerations from 0.25 to 1.4 m/s^2 from a 250-μm SET (Fig. 5). Below 2 mg/mL concentrations, particle droplets remained docked regardless of diameter. Similar to the particle containing droplets, droplet undocking using salt-based actuation was contingent upon salt concentration and SET diameter. For the smallest SET (i.e., 250 μm) it was not possible to undock droplets regardless of volume using 1 M salt solution. For 1.5 M salt solution, all droplets but 10 μL were undocked. These droplets however, at all accelerations disengaged from the magnet immediately following undocking. For 2, 2.5, and 3 M salt concentrations, only 10-μL droplets could be undocked from the SET without being disengaged from the magnet. For 3.5 M salt concentration, 10- and 20-μL droplets and for 4 M salt all droplet volumes examined could be undocked from the SET without being disengaged from the magnet. The 250-μm-diameter SETs were used to design an automated DNA fluorescence assay that allowed the droplets to be undocked, mixed, and subsequently interrogated.

DNA quantitation using fluorescence

The UED coating showed the best performance for droplet actuation of the SH materials tested (Sects. "Docking and

Fig. 5 Time lapse images of magnetic action for 20-µL droplet containing 3 mg/mL particles that merge with 5-µL green dye droplets and then undock from 250-µm SETs. Dashed arrows show direction of the droplet movement. Scale bar is 1 cm. SETs are highlighted as black dots in **d**

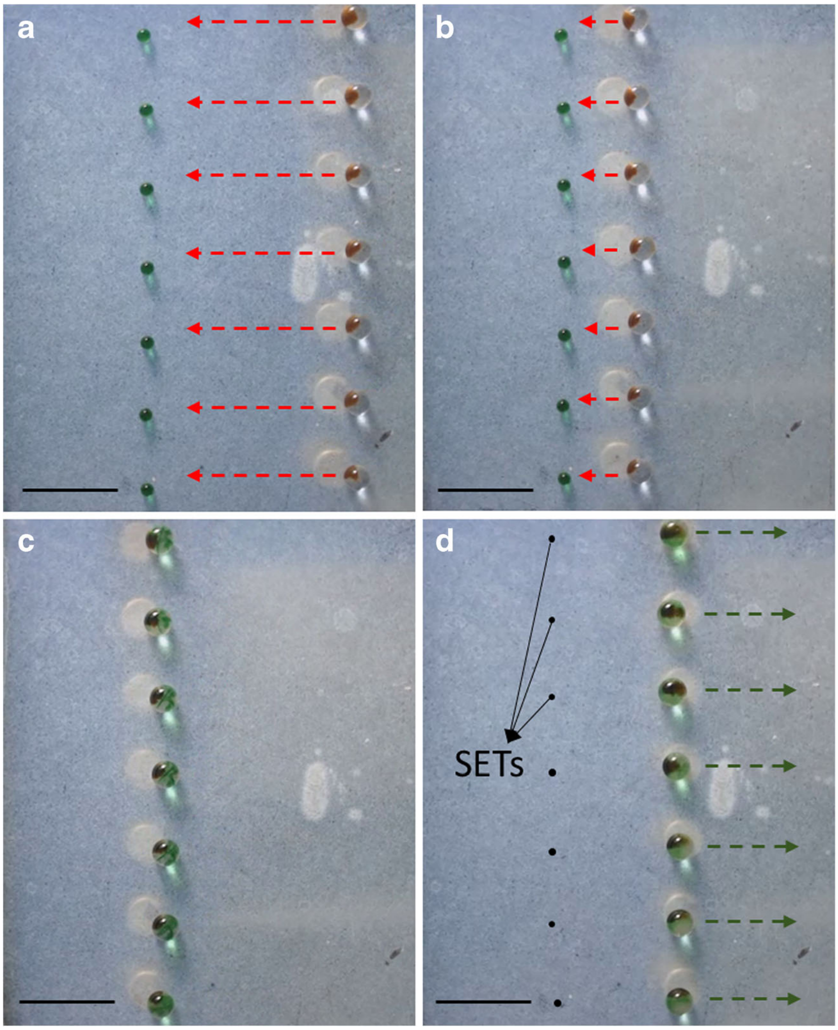

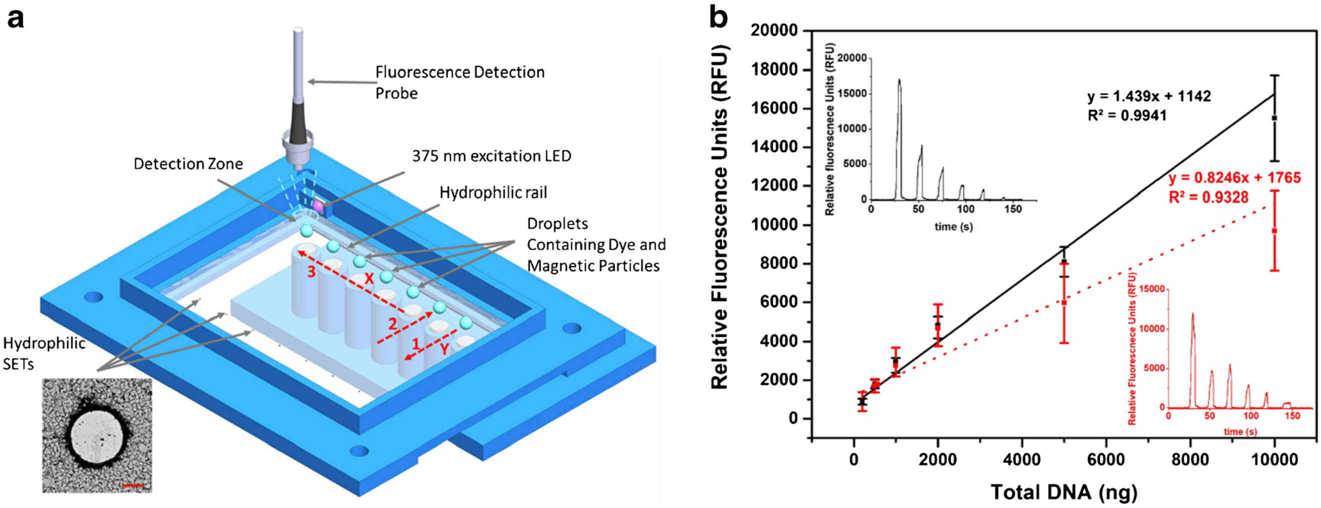

Fig. 6 **a** Schematic of the 3D-printed device used for fluorescence DNA quantitation and SH substrate which contains seven laser-micromachined 250-µm SETs. Scale bar for the inset SEM is 100 µm. Red numbers and dashed lines represent the movement direction and sequence for all the droplets simultaneously. Step 1: DNA sample is actuated to the intercalating dye droplet for mixing. Step 2: Removal of the labelled DNA droplet from the SET. Step 3: Delivery of the mixed DNA samples to the detection zone for analysis. The horizontal and vertical movement direction of magnet movement is labelled as X and Y, respectively. **b** Standard curve generated using droplet-based fluorescence detection for DNA quantitation. Insets are examples of fluorescence response generated from the spectrometer with (black) and without (red) the use of a hydrodynamic rail

undocking droplets from SETs" and "DNA quantitation using fluorescence") and the particle-based actuation exhibited a broader dynamic range in concentration with limited interference in the way of fluorescence quenching compared to magnetic salts [26]. A DNA quantitation assay was performed using UED coated on a large microscope slide with seven ablated 250-μm circular SETs (Fig. 6a). A seven-element linear permanent magnet array was mounted to the stage (below the substrate) to facilitate automated sequential droplet transport. An LED matching the Hoechst dye excitation region (375 nm) was mounted orthogonally to a collection fiber on a 3D-printed substrate holder (Fig. 6a). Individual droplets (20 μL) containing particles and DNA were dispensed on the SH surface directly above each of the magnets. Custom coding produced desired droplet motion toward the SETs to merge DNA containing droplets with the "docked" 1-μL intercalating dye droplets. The individual merged droplets (21 μL) were then undocked from the patch and then mixed while being accelerated at 0.2 m/s^2 to a velocity of 0.5 m/s and translated across the substrate and decelerated at 0.2 m/s^2. The undocking action generates a "wobble" which contributed to reagent mixing in the droplet. The droplet volume remaining at the 100-μm SETs was characterized to be 400 pL by Bachus et al. [19]. As this volume of leftover dye is significantly smaller than the initially docked dye (1 μL), this volume was negated from further calculations. The stage and magnet array were programmed so that the resultant droplets moved sequentially through the detection zone. The emission intensity of each droplet was monitored at 480 nm and averaged over triplicate measurements to generate a calibration curve for calf thymus DNA (Fig. 6b). DNA was tested over the range of 200 to 10,000 ng, and a blank correction was applied to all the samples by subtracting fluorescence of a droplet without DNA. All droplets were translated through the detection zone at a constant velocity to ensure reproducible excitation/detection time (see ESM-1 Fig. S3).

Initial experiments showed a relatively weak correlation and significant variability between relative fluorescence intensity and the DNA concentration (an example is shown as the red curve in Fig. 6b). It was suspected that variation in droplet

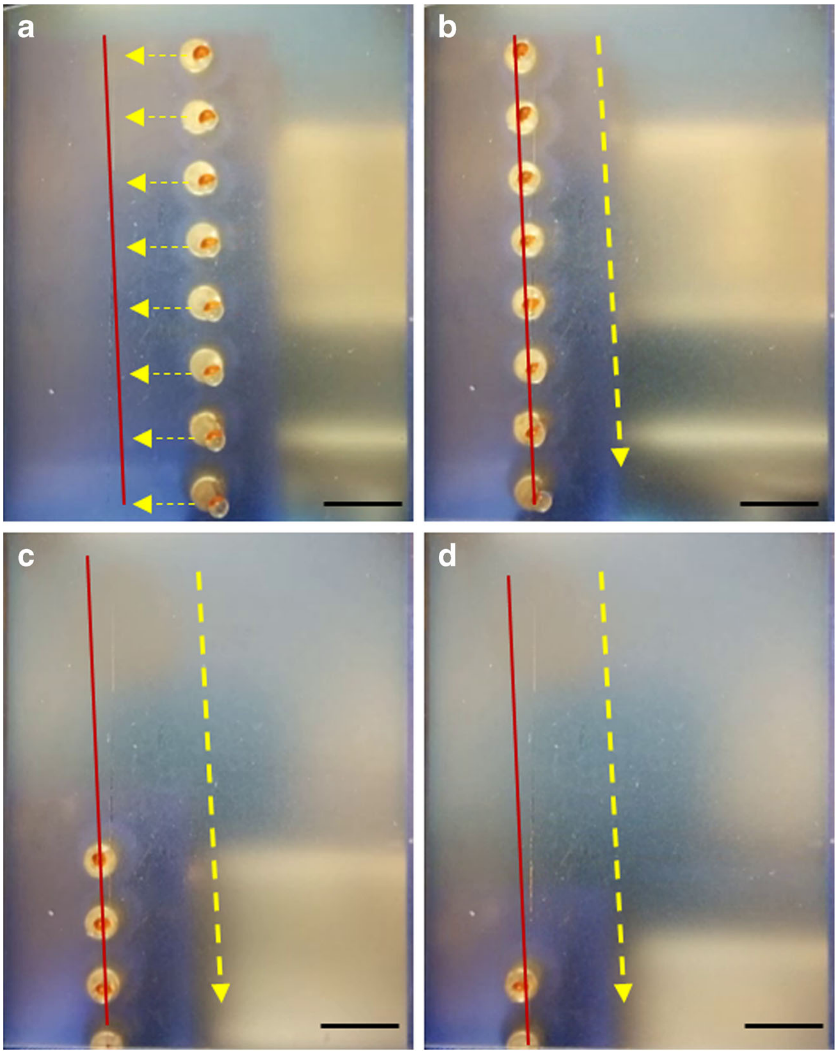

Fig. 7 Magnetic droplet actuation on a laser-micromachined "rail" for improved fluorescence signal consistency. The red solid line shows the position of the rail and yellow dashed lines show the direction of droplet movement. Scale bar is 1 cm

position within the detection zone was causing significant differences in the fluorescence emission and collection. A hydrophilic rail was laser micromachined into the surface acting as a continual SET in the 'Y' direction, which improves the linear correlation between relative fluorescence intensity and DNA (see ESM-5 and Fig. 7).

The improvement in linear correlation with the use of hydrophilic rail is exemplified by the black curve (R^2 of 0.9941) in Fig. 6b. The calibration was carried out from highest to lowest DNA concentration to probe for carryover. The improved liner correlation suggests minimal carryover by droplets on the rail. In comparison to the standard method of performing the assay, the total time is reduced from 20 mins to 1–2 min. Furthermore, sample volumes are significantly reduced from the standard 2 mL dye and 10 μL DNA to 20 μL dye and 1 μL DNA with the chip method. In addition to water droplets we have also been able to actuate 50% methanol (37.41 mN/m), 30% ethanol (35.99 mN/m), 50% ACN (37.21 mN/m), and ethylene glycol (47.31 mN/m) droplets on the SH surface using particles. A more comprehensive study is, however, required to examine the effects of solution viscosity which has been shown to cause particle loss during droplet actuation [30]. The ability to actuate liquids other than water expands and validates the use of this platform beyond water droplets.

Conclusions

(Super)hydrophobic materials including a commercial (silica nanoparticle-based) and custom synthesized porous polymer monolith (high and low density as well as fluorinated and fluorine-free) were systematically examined with magnetic actuation. Both particle and paramagnetic salt-laden droplets were actuated on each surface with increasing acceleration and deceleration, and droplet disengagement noted. Both salt and particle-based actuations were possible over a broad set of conditions (e.g., droplet volume, paramagnetic material concentration, acceleration/deceleration). Porous polymer monolithic materials are compatible with paramagnetic salt-based actuation. However, droplets containing particles are not actuated, and after magnetic field application, the particle-laden droplets become pinned. Surface energy traps can be fabricated by laser micromachining a coated surface to expose the hydrophilic glass substrate. The SETs are used to dock an aqueous droplet temporarily. A parameter space is explored conditions identified that facilitate droplet docking/undocking. A digital microfluidic platform is constructed that utilizes an array of permanent rare earth magnets for droplet actuation and LED/fiber coupled collection for detection. The magnetic array is used to carry out a rapid droplet-based fluorescence DNA assay. A laser-machined fluidic rail provides better linearity stemming from improved droplet positioning as the droplet transits the detection region. The novel feature of this platform comes from the ability to pick up parked droplets which may allow us to do chemical reactions on-chip and combine it with on-line fluorescence detection.

Acknowledgements The authors would like to extend their gratitude to Dr. Guojun Liu's research group at Queen's University for assisting with contact angle measurements and NanoFabrication Kingston where the laser micromachining was performed. The authors would also like to acknowledge the funding bodies, namely CMC Microsystems for its microfabrication support, the Canadian Foundation for Innovation (emSYSCAN Project) for infrastructure (XY gantry), and Natural Sciences and Engineering Research Council for Discovery Grant Funding.

Compliance with ethical standards

Conflict of interest The authors declare that they have no conflict of interest.

References

1. Chu Z, Seeger S. Superamphiphobic surfaces. Chem Soc Rev. 2014;43(8):2784–98. https://doi.org/10.1039/c3cs60415b.
2. Barthlott W, Neinhuis C. Purity of the sacred lotus, or escape from contamination in biological surfaces. Planta. 1997;202(1):1–8. https://doi.org/10.1007/s004250050096.
3. Golovin K, Boban M, Mabry JM, Tuteja A. Designing self-healing superhydrophobic surfaces with exceptional mechanical durability. ACS Appl Mater Interfaces. 2017;9(12):11212–23. https://doi.org/10.1021/acsami.6b15491.
4. Wang W, Lockwood K, Boyd LM, Davidson MD, Movafaghi S, Vahabi H, et al. Superhydrophobic coatings with edible materials. ACS Appl Mater Interfaces. 2016;8(29):18664–8. https://doi.org/10.1021/acsami.6b06958.
5. Han JT, Zheng Y, Cho JH, Xu X, Cho K. Stable superhydrophobic organic−inorganic hybrid films by electrostatic self-assembly. J Phys Chem B. 2005;109(44):20773–8.
6. Zhao N, Shi F, Wang Z, Zhang X. Combining layer-by-layer assembly with electrodeposition of silver aggregates for fabricating superhydrophobic surfaces. Langmuir. 2005;21(10):4713–6.
7. Han JT, Lee DH, Ryu CY, Cho K. Fabrication of superhydrophobic surface from a supramolecular organosilane with quadruple hydrogen bonding. J Am Chem Soc. 2004;126(15):4796–7.
8. Sun M, Luo C, Xu L, Ji H, Ouyang Q, Yu D, et al. Artificial lotus leaf by nanocasting. Langmuir. 2005;21(19):8978–81.
9. Lee W, Jin M-K, Yoo W-C, Lee J-K. Nanostructuring of a polymeric substrate with well-defined nanometer-scale topography and tailored surface wettability. Langmuir. 2004;20(18):7665–9.
10. Auad P, Ueda E, Levkin PA. Facile and multiple replication of superhydrophilic–superhydrophobic patterns using adhesive tape. ACS Appl Mater Interfaces. 2013;5(16):8053–7. https://doi.org/10.1021/am402135e.
11. Ueda E, Levkin PA. Emerging applications of superhydrophilic-superhydrophobic micropatterns. Adv Mater. 2013;25(9):1234–47. https://doi.org/10.1002/adma.201204120.
12. Feng W, Li L, Ueda E, Li J, Heißler S, Welle A, et al. Surface patterning via thiol-yne click chemistry: an extremely fast and versatile approach to superhydrophilic-superhydrophobic micropatterns. Adv Mater Interfaces. 2014;1(7):1400269. https://doi.org/10.1002/admi.201400269.

13. Levkin PA, Svec F, Frechet JMJ. Porous polymer coatings: a versatile approach to superhydrophobic surfaces. Adv Funct Mater. 2009;19(12):1993–8. https://doi.org/10.1002/adfm.200801916.
14. Jebrail MJ, Wheeler AR. Let's get digital: digitizing chemical biology with microfluidics. Curr Opin Chem Biol. 2010;14(5):574–81. https://doi.org/10.1016/j.cbpa.2010.06.187.
15. Hirai Y, Mayama H, Matsuo Y, Shimomura M. Uphill water transport on a wettability-patterned surface: experimental and theoretical results. ACS Appl Mater Interfaces. 2017;9(18):15814–21. https://doi.org/10.1021/acsami.7b00806.
16. Wang S, Liu K, Yao X, Jiang L. Bioinspired surfaces with super wettability: new insight on theory, design, and applications. Chem Rev. 2015;115(16):8230–93. https://doi.org/10.1021/cr400083y.
17. Tenjimbayashi M, Higashi M, Yamazaki T, Takenaka I, Matsubayashi T, Moriya T, et al. Droplet motion control on dynamically hydrophobic patterned surfaces as multifunctional liquid manipulators. ACS Appl Mater Interfaces. 2017;9(12):10371–7. https://doi.org/10.1021/acsami.7b01641.
18. Bachus K. Engineering patterned materials and microstructured fibers for microfluidics and analytical applications. PhD dissertation. Kigston: Queen's University; 2017.
19. Bachus KJ, Mats L, Choi HW, Gibson GTT, Oleschuk RD. Fabrication of patterned superhydrophobic/hydrophilic substrates by laser micromachining for small volume deposition and droplet-based fluorescence. ACS Appl Mater Interfaces. 2017;9(8):7629–36. https://doi.org/10.1021/acsami.6b16363.
20. Sekula-Neuner S, de Freitas M, Tröster L-M, Jochum T, Levkin PA, Hirtz M, Fuchs H. Phospholipid arrays on porous polymer coatings generated by micro-contact spotting. Beilstein J Nanotechnol. 2017;8:715–22.
21. Ueda E, Geyer FL, Nedashkivska V, Levkin PA. Droplet microarray: facile formation of arrays of microdroplets and hydrogel micropads for cell screening applications. Lab Chip. 2012;12(24):5218–24. https://doi.org/10.1039/C2LC40921F.
22. Sackmann EK, Fulton AL, Beebe DJ. The present and future role of microfluidics in biomedical research. Nature. 2014;507(7491):181–9. https://doi.org/10.1038/nature13118.
23. Decrop D, Pardon G, Brancato L, Kil D, Zandi Shafagh R, Kokalj T, et al. Single-step imprinting of femtoliter microwell arrays allows digital bioassays with attomolar limit of detection. ACS Appl Mater Interfaces. 2017;9(12):10418–26. https://doi.org/10.1021/acsami.6b15415.
24. Ng AHC, Choi K, Luoma RP, Robinson JM, Wheeler AR. Digital microfluidic magnetic separation for particle-based immunoassays. Anal Chem. 2012;84(20):8805–12. https://doi.org/10.1021/ac3020627.
25. Zhang Y, Nguyen N-T. Magnetic digital microfluidics - a review. Lab Chip. 2017;17(6):994–1008. https://doi.org/10.1039/C7LC00025A.
26. Mats L. Continuous and digital approaches to manipulation and detection of analytes on microfluidic devices. Queen's University; 2016.
27. Mats L, Young R, Gibson GTT, Oleschuk RD. Magnetic droplet actuation on natural (Colocasia leaf) and fluorinated silica nanoparticle super hydrophobic surfaces. Sensors Actuators B Chem. 2015;220:5–12. https://doi.org/10.1016/j.snb.2015.05.027.
28. Nguyen NT, Zhu G, Chua YC, Phan VN, Tan SH. Magneto wetting and sliding motion of a sessile ferrofluid droplet in the presence of a permanent magnet. Langmuir. 2010;26(15):12553–9. https://doi.org/10.1021/la101474e.
29. Guo Z-G, Zhou F, Hao J-C, Liang Y-M, Liu W-M, Huck WTS. "Stick and slide" ferrofluidic droplets on superhydrophobic surfaces. Appl Phys Lett. 2006;89(8):081911. https://doi.org/10.1063/1.2336729.
30. Long Z, Shetty AM, Solomon MJ, Larson RG. Fundamentals of magnet-actuated droplet manipulation on an open hydrophobic surface. Lab Chip. 2009;9(11):1567–75. https://doi.org/10.1039/b819818g.
31. Cesarone CF, Bolognesi C, Santi L. Improved microfluorometric DNA determination in biological material using 33258 Hoechst. Anal Biochem. 1979;100(1):188–97. https://doi.org/10.1016/0003-2697(79)90131-3.
32. Labarca C, Paigen K. A simple, rapid, and sensitive DNA assay procedure. Anal Biochem. 1980;102(2):344–52. https://doi.org/10.1016/0003-2697(80)90165-7.
33. Daxhelet GA, Coene MM, Hoet PP, Cocito CG. Spectrofluorometry of dyes with DNAs of different base composition and conformation. Anal Biochem. 1989;179(2):401–3. https://doi.org/10.1016/0003-2697(89)90152-8.
34. Moe D, Garbarsch C, Kirkeby S. The protein effect on determination of DNA with Hoechst 33258. J Biochem Biophys Methods. 1994;28(4):263–76. https://doi.org/10.1016/0165-022X(94)90002-7.
35. Stout D, Becker F. Fluorometric quantitation of single-stranded DNA: a method applicable to the technique of alkaline elution. Anal Biochem. 1982;127(2):302–7.
36. Chen J, Ji X, He Z. High-throughput droplet analysis and multiplex DNA detection in the microfluidic platform equipped with a robust sample-introduction technique. Anal Chim Acta. 2015;888:110–7. https://doi.org/10.1016/j.aca.2015.07.054.
37. Svec F. Porous polymer monoliths: amazingly wide variety of techniques enabling their preparation. J Chromatogr A. 2010;1217(6):902–24.
38. Bachus KJ, Langille KJ, Fu Y, Gibson GTT, Oleschuk RD. Controlling the morphology of (concentric) microtubes formed by in situ free radical polymerization. Polymer. 2015;58:113–20. https://doi.org/10.1016/j.polymer.2014.12.040.
39. Fu Y, Gibson GTT, Oleschuk RD. Polymer microstructures with high aspect ratio and low polydispersity using photonic fibres as templates. J Mater Chem. 2012;22(17):8208–14. https://doi.org/10.1039/C2JM16752B.
40. Egatz-Gómez A, Melle S, García AA, Lindsay SA, Márquez M, Domínguez-García P, et al. Discrete magnetic microfluidics. Appl Phys Lett. 2006;89(3):034106. https://doi.org/10.1063/1.2227517.
41. García AA, Egatz-Gómez A, Lindsay SA, Domínguez-García P, Melle S, Marquez M, et al. Magnetic movement of biological fluid droplets. J Magn Magn Mater. 2007;311(1):238–43. https://doi.org/10.1016/j.jmmm.2006.10.1149.
42. Hutama TJ, Oleschuk RD. Magnetically manipulated droplet splitting on a 3D-printed device to carry out a complexometric assay. Lab Chip. 2017;17(15):2640–9. https://doi.org/10.1039/C7LC00629B.